Stereoelectronic Factors That Influence Kinetic and Thermodynamic Sites of Protonation of (η^6-Arene)molybdenum(phosphine)$_3$ Complexes

Michael T. Ashby,* Victor S. Asirvatham, Angela S. Kowalski, and Masood A. Khan

Department of Chemistry and Biochemistry, The University of Oklahoma, 620 Parrington Oval, Rm. 208, Norman, Oklahoma 73019

Received April 21, 1999

We have previously reported (*J. Am. Chem. Soc.* **1995**, *117*, 12639) the arene complex (η^6-C_6H_6)Mo(TRIPOD) (**1**), where TRIPOD = 1,1,1-tris(diphenylphosphinomethyl)ethane, is protonated upon addition of 1 equiv of D^+ to yield the metal−hydride [(η^6-C_6H_5D)Mo(TRIPOD)H]$^+$ (**1H$^+$-d$_1$**) via *exo* addition of D^+ to the arene ligand followed by migration to the metal of the *endo* proton of the putative η^5-cyclohexadienyl complex [(η^5-C_6H_6D)Mo(TRIPOD)]$^+$ (**1‡**). The opposite isotopomer is obtained when (η^6-C_6D_6)Mo(TRIPOD) (**1-d$_6$**) is employed to give [(η^6-C_6D_5H)Mo(TRIPOD)D]$^+$ (**1D$^+$-d$_6$**). Our recent investigation of the electronic structure of **1** and its one-electron oxidized derivative [(η^6-C_6H_6)Mo(TRIPOD)]$^+$ (**1**$^+$) suggested the mechanism of protonation is not driven entirely by electronic factors; steric factors are likely important for indirect protonation of **1**. Consistent with that conclusion, we report herein that some other phosphine derivatives are protonated directly at the metal center. Thus, under the same reaction conditions the monodentate phosphine derivatives (η^6-C_6D_6)Mo(PR_3)$_3$, where PR_3 = PPh_2Me (**3-d$_6$**), $PPhMe_2$ (**4-d$_6$**), and PMe_3 (**5-d$_6$**), are protonated directly at the metal 0%, 20%, and 40% of the time, respectively. The remainder of the protonations take place via the aforementioned indirect protonation of the arene ligand. Surprisingly, (η^6-C_6D_6)Mo(TRIPHOS) (**2-d$_6$**), where TRIPHOS = bis(2-diphenylphosphinoethyl)phenylphosphine, reacts with H^+ by direct protonation of the metal center 80% of the time to give a C_1-symmetric kinetic hydride [(η^6-C_6D_6)Mo(TRIPHOS)H]$^+$ (**2$_K$H$^+$-d$_6$**). The other 20% of the time **2-d$_6$** reacts via the arene mechanism to give [(η^6-C_6D_5H)Mo(TRIPHOS)D]$^+$ (**2$_K$D$^+$-d$_6$**). The two enantiomeric forms of **2$_K$H$^+$** are observed to be in rapid equilibrium ($k = 6.4 \times 10^3$ s^{-1} at −87 °C). Compound **2$_K$H$^+$** eventually isomerizes ($k = 6.1 \times 10^{-4}$ s^{-1} at −60 °C) to the C_s-symmetric thermodynamic hydride [(η^6-C_6H_6)Mo(TRIPHOS)H]$^+$ (**2$_T$H$^+$**). We conclude from the crystal structures of **1**−**4**, tracer studies, and electronic structure calculations of the five derivatives **1**−**5** presented herein that indirect protonation does not represent a general mechanism for this class of compounds. In addition to electronic factors that favor direct protonation of the metal center from an equatorial trajectory, subtle steric demands of the phosphine ligands play an important role in dictating whether a proton initially attacks the arene ligand or the metal of **1**−**5**. The semiempirical PM3(tm) method may be used to map metal-based frontier orbitals of the complexes **1**−**5** onto plots of their surface electron densities, thereby revealing sterically accessible metal electron density. Such plots provide straightforward models that predict the mechanisms of protonation.

Introduction

Protonation of a metal, the simplest electrophilic reaction, is a chemical modification that results in a change in the formal oxidation state of the metal center without altering its electron count. One impetus for studying such reactions is that some biological pathways likely involve protonation of metal centers of metalloproteins.[1] For example, some isoforms of metallohydrogenases have been optimized to reduce protons. Protonation of metal complexes is also invoked in catalytic processes that have been devised by Man[2] such as the hydrogenation of unsaturated organic substrates by metal complexes that activate molecular hydrogen heterolytically.[3] The issue of protonation of metal centers versus ligand sites under thermodynamic conditions has been raised before,[4,5] and in a few cases rearrangement of kinetic and thermodynamic protonation products has

(1) Evans, D. J.; Henderson, R. A.; Smith, B. E. In *Catalysis by Nitrogenases and Synthetic Analogues*; Reedijk, J., Ed.; Marcel Dekker: New York, 1993; pp 89−130.

(2) Gates, B. C. *Catalytic Chemistry*; John Wiley: New York, 1991.

(3) James, B. R.; Ashby, M. T. In *Inorganic Reactions and Methods*; Norman, A., Ed.; VCH: Weinheim, 1993; Vol. 16, pp 71−76.

(4) Kristjánsdóttir, S. S.; Norton, J. R. In *Transition Metal Hydrides*; Dedieu, A., Ed.; VCH: Weinheim, 1992; pp 309−359.

(5) Regioselective protonation of unsaturated hydrocarbon ligands (but not arenes) has been reviewed: Henderson, R. A. *Angew. Chem., Int. Ed. Engl.* **1996**, *35*, 946−967.

10.1021/om990281n CCC: $18.00
Publication on Web 11/02/1999

Chart 1

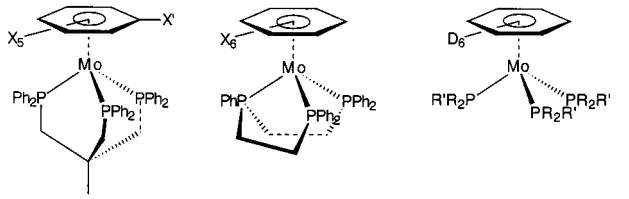

1 (X=X'=H)
1-d_1 (X=H,X'=D)
1-d_5 (X=D,X'=H)
1-d_6 (X=X'=D)

2(X=H)
2-d_6 (X=D)

3-d_6 (R=Ph,R'=Me)
4-d_6 (R=Me,R'=Ph)
5-d_6 (R=R'=Me)

been studied.[6−8] We reported in a communication that the arene complex (η^6-C_6H_6)Mo(TRIPOD) (**1**) is protonated via *exo* addition of H^+ to the arene ligand to give a transient η^5-cyclohexadienyl complex [(η^5-C_6H_7)Mo(TRIPOD)]$^+$ (**1**‡) that yields the metal−hydride (η^6-C_6H_6)Mo(TRIPOD)(H)]$^+$ (**1H**$^+$) by *endo* hydrogen atom transfer to the metal (Figure 5).[9] Prompted by our recent study of the electronic structure of **1** that suggested steric factors might be important,[10] we now present a full account of the earlier mechanistic investigation of the protonation of **1** as well as related studies for the derivatives (η^6-C_6H_6)Mo(TRIPHOS) (**2**), (η^6-C_6H_6)Mo(PPh_2Me)$_3$ (**3**), (η^6-C_6H_6)Mo($PPhMe_2$)$_3$ (**4**), and (η^6-C_6H_6)Mo(PMe_3)$_3$ (**5**) (Chart 1), some of which react via direct attack on the metal. A balance between steric factors that are related more to the conformations of the phosphine ligands than their substitution patterns and the spatial nature of the metal-based frontier orbitals is found to dictate the initial sites of protonation in these complexes.

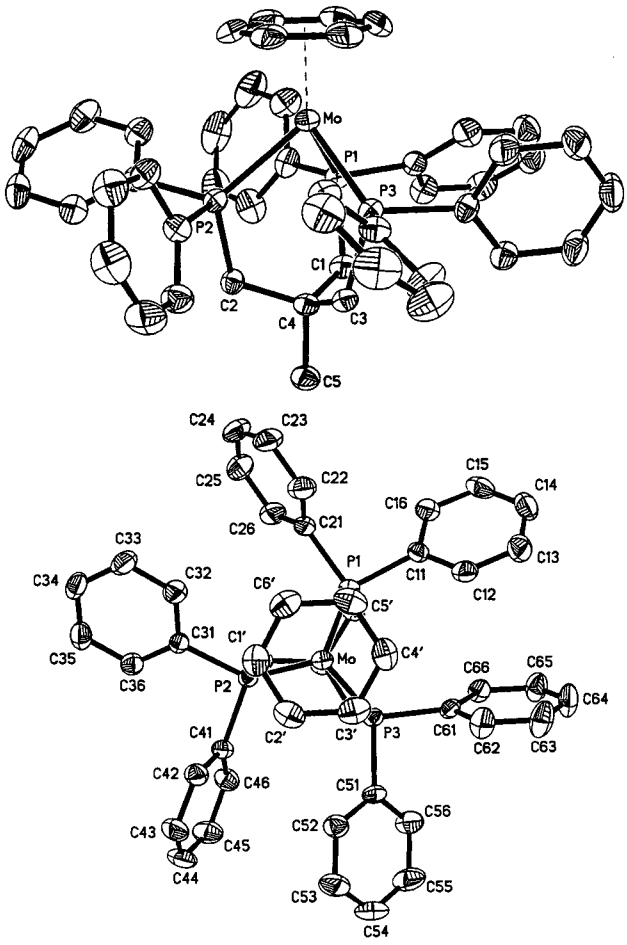

Figure 1. Thermal ellipsoid drawing (50% probability) of (η^6-C_6H_6)Mo(TRIPOD) (**1**) from the top and the side with the labeling scheme.

Experimental Section

Chemicals and Solvents. All operations were carried out using Schlenk or glovebox techniques under argon or nitrogen. Hydrocarbon solvents were distilled from sodium/benzophenone ketal, CH_2Cl_2 was distilled from CaH_2, and methanol was refluxed over Mg and distilled.[11] All solvents were degassed by three freeze−pump−thaw cycles before use. The phosphine ligands were used as received from Aldrich and Strem Chemicals. (η^6-C_6H_6)$_2$Mo[12] and $CDCl_3F$[13] were synthesized according to published procedures.

Instruments and References. ^{1}H, ^{2}H, and ^{31}P NMR spectra were recorded on a Varian XL-500 spectrometer. The NMR samples were prepared in tubes that had been glass-blown onto Schlenk adapters. The solutions were freeze−pump−thawed before the tubes were flame-sealed under vacuum. ^{1}H NMR spectra were referenced to residual solvent peaks $CDHCl_2$ (5.32 ppm), $CHCl_2F$ (7.47 ppm, d, J_{H-F} = 50 Hz), and C_6D_5H (7.24 ppm). ^{2}H NMR spectra were referenced to the corresponding ^{1}H NMR chemical shifts. ^{31}P NMR spectra were referenced to external 85% H_3PO_4. Combustion analyses were performed by Midwest Microlabs, Indianapolis, IN. Calculations were performed on a Silicon Graphics IRIS Indigo 2 Solid Impact.

Synthesis of (η^6-C_6H_6)Mo(TRIPOD) (1) and Its d_6 Isotopomer from a Melt Reaction. (η^6-C_6H_6)$_2$Mo (0.34 g, 1.35 mmol) and TRIPOD (0.76 g, 1.22 mmol) were heated in a sealed glass tube under vacuum at 160 °C for 48 h. The tube was opened under nitrogen, the contents were extracted with 1:1 benzene/heptane (∼30 mL), and the extract was filtered. The red-orange product crystallized from the solvent upon cooling to 5 °C (0.62 g, 64%). ^{1}H NMR (C_6D_6, 500 MHz, 20 °C): δ 7.08 (m, 12 H, Ph) 6.96 (t, 6 H, J = 7 Hz, Ph), 6.85 (t, 12 H, J = 7 Hz, Ph), 4.41 (m, 6 H, C_6H_6), 2.17 (m, 6 H, CH_2), 1.16 (m, 3 H, CH_3). ^{31}P{^{1}H} NMR (C_6D_6, 202 MHz, 20 °C): δ 46.59 (s). Anal. Calcd (found) for $C_{47}H_{45}P_3Mo$ (798.74): C, 70.68 (70.44), H, 5.68 (5.74). The isotopomer (η^6-C_6D_6)Mo(TRIPOD) (**1-d_6**) was synthesized using the same procedure with (C_6D_6)$_2$-Mo in 61% yield. ^{1}H NMR (C_6D_6, 500 MHz, 20 °C) the same as **1** except: δ 4.41 (m, 0.21 H, C_6H_6).

General Synthesis of (η^6-C_6H_6)Mo(P)$_3$ and Their d_6 Isotopomers from Solution Reactions: 2 ((P)$_3$ = TRIPHOS), 3 (P = PPh_2Me), 4 (P = $PPhMe_2$), 5 (P = PMe_3). The procedure used to synthesize **2** is typical. (η^6-C_6H_6)$_2$Mo (0.20 g, 0.78 mmol) and TRIPHOS (0.40 g, 0.75 mmol) were dissolved in benzene (10 mL). The flask was frozen, evacuated, and sealed before heating in an oil bath at 160 °C for 24 h. The flask was backfilled with Ar, methanol (30 mL) was layered over the red-brown solution, and the flask was placed in a refrigerator at 5 °C for 12 h to yield **2** (0.32 g, 59%) as red-orange crystals. The isotopomers **2-d_6**, **3-d_6**, **4-d_6**, and **5-d_6** were synthesized using a similar procedure from (η^6-C_6D_6)$_2$-

(6) Darensbourg, M. Y.; Liaw, W. F.; Riordan, C. G. *J. Am. Chem. Soc.* **1989**, *111*, 8051.
(7) Gladfelter, W. L.; Stevens, R. E. *J. Am. Chem. Soc.* **1982**, *104*, 6454.
(8) Stevens, R. E.; Guettler, R. D.; Gladfelter, W. L. *Inorg. Chem.* **1990**, *29*, 451.
(9) Kowalski, A. S.; Ashby, M. T. *J. Am. Chem. Soc.* **1995**, *117*, 12639.
(10) Asirvatham, V. S.; Gruhn, N. E.; Lichtenberger, D. L.; Ashby, M. T. *Organometallics*, submitted for publication.
(11) Perrin, D. D.; Armarego, W. L. F. *Purification of Laboratory Chemicals*, 3rd ed.; Pergamon: Oxford, 1988.
(12) Silverthorn, W. E. *Inorg. Synth.* **1977**, *17*, 54.
(13) Siegel, J. S.; Anet, F. A. L. *J. Org. Chem.* **1988**, *53*, 2629.

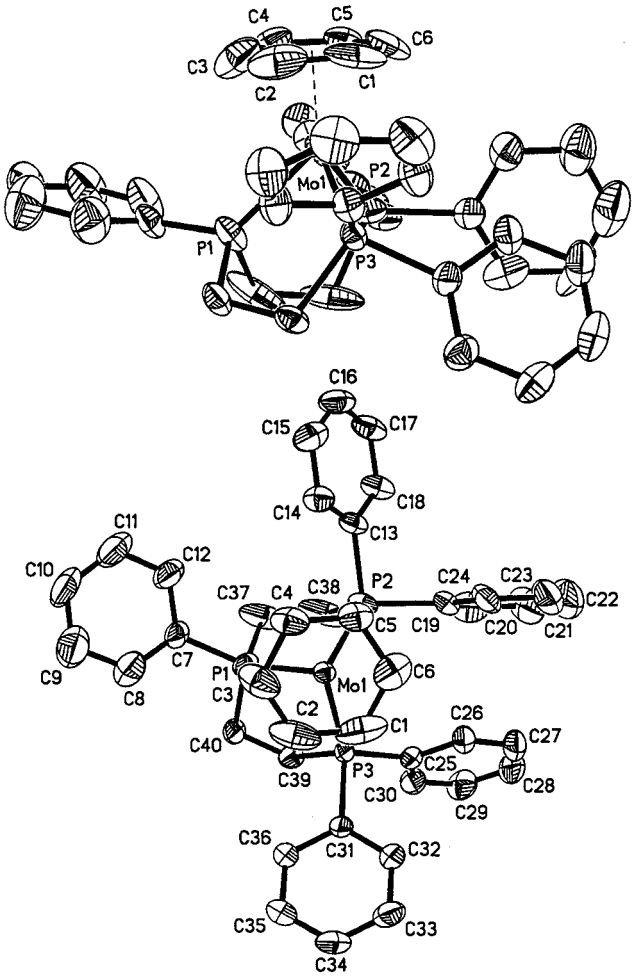

Figure 2. Thermal ellipsoid drawing (50% probability) of (η^6-C_6H_6)Mo(TRIPHOS) (**2**) from the top and the side with the labeling scheme.

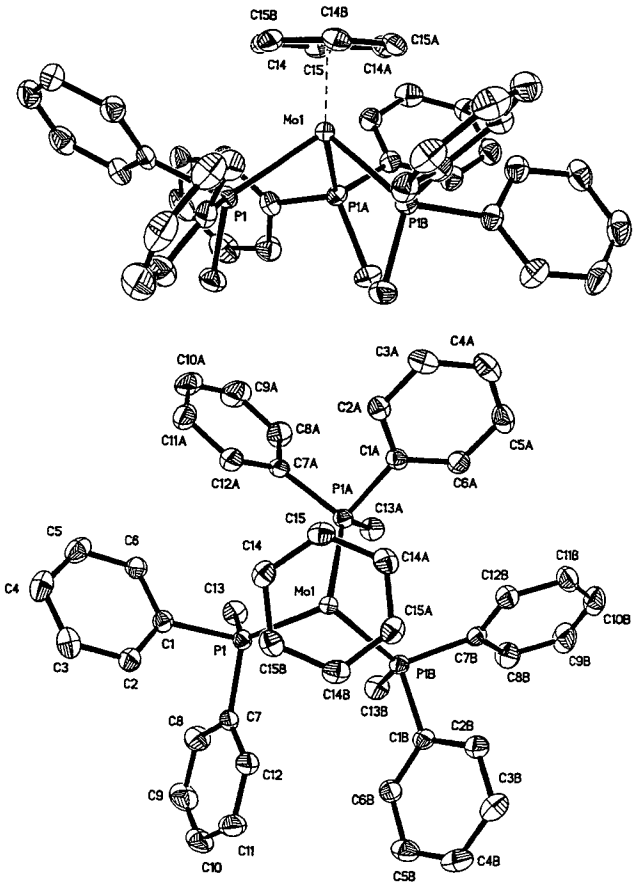

Figure 3. Thermal ellipsoid drawing (50% probability) of (η^6-C_6H_6)Mo(PPh_2Me)$_3$ (**3**) from the top and the side with the labeling scheme.

Mo and C_6D_6 as a solvent. The known compounds **2**−**5** and their isotopomers were characterized spectroscopically.

For **2-d$_6$** (59% yield): ^{1}H NMR (C_6D_6, 500 MHz, 20 °C) δ 7.95 (m, 2 H, Ph), 7.36 (m, 2 H, Ph), 7.12−7.24 (m, 11 H, Ph), 7.00 (m, 2 H, Ph), 6.84−6.94 (m, 8 H, Ph), 4.09 (m, 0.19 H, C_6D_5H) 2.14 (m, 4 H, CH_2) 1.68 (m, 2 H, CH_2) 0.78 (m, 2 H, CH_2); ^{31}P{^{1}H} NMR (C_6D_6, 202 MHz, 20 °C) δ 104.8 (t, 1 P, J_{P-P} = 17 Hz) 87.9 (d, 2 P).

For **3-d$_6$** (61% yield): ^{1}H NMR (C_6D_6, 500 MHz, 20 °C) δ 6.93−7.21 (m, 30 H, Ph), 3.88 (m, 0.23 H, C_6D_5H), 1.65 (s, 9 H, CH_3); ^{31}P{^{1}H} NMR (C_6D_6, 202 MHz, 20 °C) δ 35.9 (s).

For **4-d$_6$** (30% yield): ^{1}H NMR (C_6D_6, 500 MHz, 20 °C) δ 7.43 (m, 6 H, Ph), 7.11 (m, 6 H, Ph), 7.04 (m, 3 H, Ph), 3.86 (m, 0.15 H, C_6D_5H) 1.29 (s, 18 H, CH_3); ^{31}P{^{1}H} NMR (C_6D_6, 202 MHz, 20 °C) δ 17.8 (s).

For **5-d$_6$** (49% yield): ^{1}H NMR (C_6D_6, 500 MHz, 20 °C) δ 3.65 (m, 0.27 H, C_6D_5H) 1.13 (s, 27 H, CH_3); ^{31}P{^{1}H} NMR (C_6D_6, 202 MHz, 20 °C) δ 3.4 (s).

General Procedure for the Synthesis of [(η^6-C_6H_6)Mo(P)$_3$H]PF_6 and Their d_6 Isotopomers: 1H$^+$ ((P)$_3$ = TRIPOD), 2$_T$H$^+$ ((P)$_3$ = TRIPHOS), 3H$^+$ (P = PPh_2Me), 4H$^+$ (P = $PPhMe_2$), 5H$^+$ (P = PMe_3). The procedure used to synthesize **1H$^{\bullet+}$PF$_6^-$** is typical. Compound **1** (0.37 g, 0.46 mmol) was dissolved in CH_2Cl_2 (10 mL), and HPF_6 (60% in water, 0.5 mL) was added. After stirring 15 min, the solution was extracted with water (2 × 10 mL) and the organic layer was dried over $CaCl_2$. Evaporation of the solvent yielded **1H$^{\bullet+}$PF$_6^-$** as a red solid that was recrystallized from CH_2Cl_2/Et_2O (0.24 g, 56%). Compound **2$_T$H$^{\bullet+}$PF$_6^-$** has been reported previously,[14] but it was not fully characterized. The spectra for **2$_K$H$^{\bullet+}$F$_3$CSO$_3^-$** in CD_2Cl_2 were obtained by in situ synthesis from **2** and F_3CSO_3H at −90 °C. The known compounds **3H$^+$**, **4H$^+$**, and **5H$^+$** were characterized spectroscopically. All of the isotopomers were characterized spectroscopically. The isotopomer distribution is given in Table 3. Static NMR spectra are obtained for **1H$^+$** and **2$_K$H$^+$** at low temperature, but dynamic spectra are observed at elevated temperatures.

For **1H$^{\bullet+}$PF$_6^-$** (56%): ^{1}H NMR ($CDCl_2F$, 500 MHz, −125 °C) δ 7.28 (m, 4 H, Ph), 7.20 (m, 4 H Ph), 7.12 (m, 6 H, Ph), 7.01 (m, 8 H, Ph), 6.90 (m, 4 H, Ph), 6.63 (m, 4 H, Ph), 5.30 (s, 6 H, C_6H_6), 2.31 (br s, 2H, CH_2), 2.19, 2.65 (br m, 4 H, diastereotopic CH_2), 1.54 (br s, 3 H, CH_3), −6.36 (td, 1 H, J_{PH} = 16 and 62 Hz, Mo−H); ^{31}P{^{1}H} NMR ($CDCl_2F$, 202 MHz, −125 °C) δ 43.2 (d, 2 P, J_{PP} = 62 Hz), 34.5 (t, 1 P); ^{1}H NMR (CD_2Cl_2, 500 MHz, 20 °C) δ 7.25 (t, 6 H, J = 7 Hz, Ph), 7.11 (t, 12 H, J = 7 Hz, Ph), 6.98 (m, 12 H, Ph), 5.24 (s, 6 H, C_6H_6), 2.41 (br s, 6 H, CH_2), 1.57 (br s, 3 H, CH_3), −6.98 (q, 1 H, J_{PH} = 45 Hz, Mo−H); ^{31}P{^{1}H} NMR (CD_2Cl_2, 202 MHz, 20 °C) δ 34.52 (s). Anal. Calcd (found) for $C_{47}H_{46}P_4F_6Mo$ (944.71): C 59.76 (59.48), H 4.91 (4.95).

For **1D$^+$-d$_6$·F$_3$CSO$_3^-$**: ^{1}H NMR (CD_2Cl_2, 500 MHz, 20 °C) δ 7.25 (t, 6 H, J = 7 Hz, Ph), 7.11 (t, 12 H, J = 7 Hz, Ph), 6.98 (m, 12 H, Ph), 5.30 (s, 1.17 H, $C_6D_5H/C_6D_4H_2$), 2.31 (br s, 6 H, CH_2), 1.54 (br s, 3 H, CH_3); ^{2}H NMR (CD_2Cl_2, 500 MHz, 20 °C) δ 5.30 (s, 4.83 D, C_6H_6), −6.98 (q, 1 H, J_{PD} = 6 Hz, Mo−D); ^{31}P{^{1}H} NMR (CD_2Cl_2, 202 MHz, 20 °C) δ 34.52 (t, J_{PD} = 6 Hz).

For **2$_T$H$^{\bullet+}$PF$_6^-$**: ^{1}H NMR (CD_2Cl_2, 500 MHz, 20 °C) δ 7.67 (m, 4 H, Ph), 7.58 (m, 1 H, Ph), 7.55 (m, 4 H, Ph), 7.33−7.43 (m, 8 H, Ph), 7.19−7.29 (m, 8 H, Ph), 4.63 (s, 6 H, C_6H_6), 2.88

(14) George, T. A.; Hammud, H. H. *J. Organomet. Chem.*, **1995**, *503*, C1.

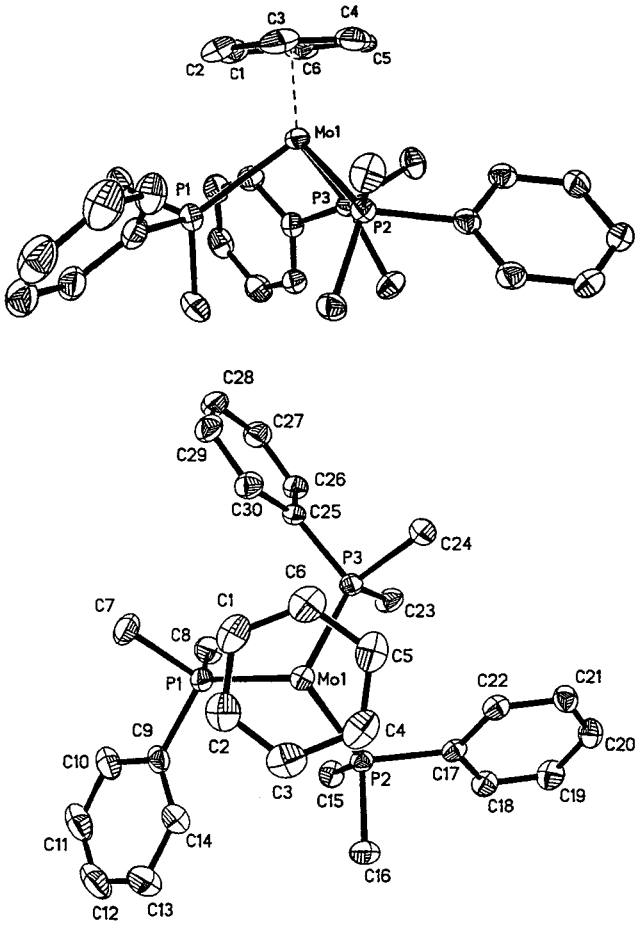

Figure 4. Thermal ellipsoid drawing (50% probability) of (η^6-C_6H_6)Mo(PPhMe$_2$)$_3$ (**4**) from the top and the side with the labeling scheme.

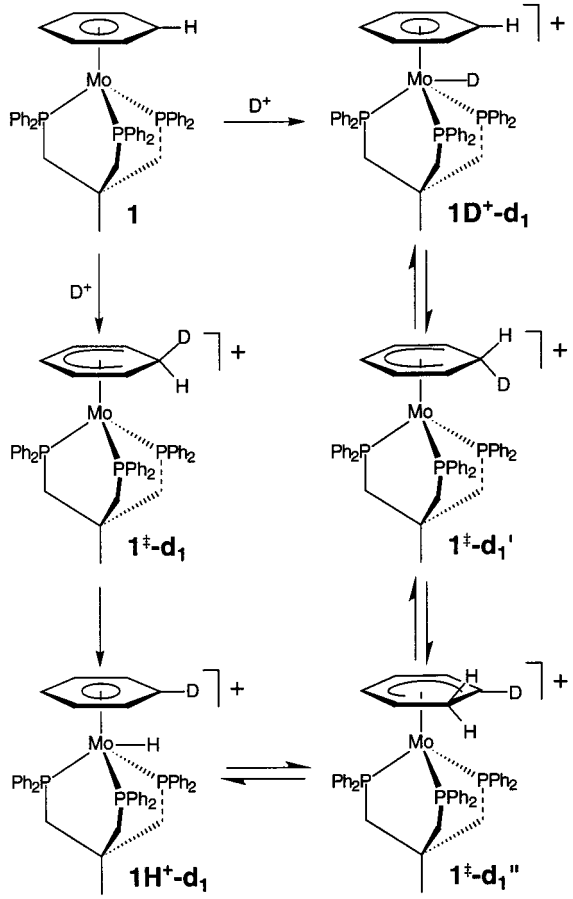

Figure 5. Kinetic products possible upon addition of D$^+$ to (η^6-C_6H_6)Mo(TRIPOD) (**1**) via (i) direct attack on the metal (**1** → **1D$^+$-d$_1$**) and (ii) indirect attack via a η^5-cyclohexadienyl ion (**1** → **1‡-d$_1$** → **1H$^+$-d$_1$**). The equilibria **1D$^+$-d$_1$** ⇌ **1‡-d$_1$′** ⇌ **1‡-d$_1$″** ⇌ **1H$^+$-d$_1$** could explain the incorporation of deuterium into the arene ligand even if the initial protonation is at the metal (**1** → **1D$^+$-d$_1$**), but selective spin inversion transfer (SSIT) NMR studies rule out such equilibria (see text). Only one arene hydrogen atom is shown for the sake of clarity.

(m, 2 H, CH_2), 2.66 (m, 2 H, CH_2), 2.12 (m, 2 H, CH_2), 2.04 (m, 2 H, CH_2), −6.06 (td, 1 H, J_{PH} = 4 and 49 Hz, Mo−H); $^{31}P\{^1H\}$ NMR (CD_2Cl_2, 202 MHz, 20 °C) δ 110.08 (t, 1 P, J_{P-P}= 32 Hz), 89.9 (d, 2 P), −144.0 (septet, 1 P, J_{P-F} = 709 Hz).

For **2$_T$H$^+$-d$_6$·F$_3$CSO$_3^-$** and **2$_T$D$^+$-d$_6$·F$_3$CSO$_3^-$**: ^1H NMR (CD_2Cl_2, 500 MHz, 20 °C) δ 7.67 (m, 4 H, Ph), 7.58 (m, 1 H, Ph), 7.55 (m, 4 H, Ph), 7.33−7.43 (m, 8 H, Ph), 7.19−7.29 (m, 8 H, Ph), 4.63 (s, 0.31 H, $C_6D_5H/C_6D_4H_2$), 2.88 (m, 2 H, CH_2), 2.66 (m, 2 H, CH_2), 2.12 (m, 2 H, CH_2), 2.04 (m, 2 H, CH_2), −6.06 (td, 0.88 H, J_{PH} = 4 and 49 Hz, Mo−H); ^2H NMR (CD_2Cl_2, 76.7 MHz, 20 °C) δ 4.63 (br m, 5.54 D, $C_6D_5H/C_6D_4H_2$), −6.06 (br m, 0.27 D, Mo−D); $^{31}P\{^1H\}$ NMR (CD_2Cl_2, 202 MHz, 20 °C) δ 110.3 (t, 0.8 P, J_{PP} = 32 Hz, $(-CH_2)_2$(Ph)P−H), 110.2 (br t, 0.2 P, J_{PP} = 32 Hz, $(-CH_2)_2$(Ph)P−D), 90.2 (d, 1.6 P, $(-CH_2)$(Ph)$_2$P−H), 90.1 (m, 0.4 P, $(-CH_2)$(Ph)$_2$P−D).

For **2$_K$H$^+$·F$_3$CSO$_3^-$**: ^1H NMR (CD_2Cl_2, 500 MHz, −90 °C) δ 8.02 (m, 2 H, Ph), 7.66 (m, 4 H, Ph), 7.34 (m, 2 H, Ph), 7.23 (m, 2 H, Ph), 7.16 (m, 4 H, Ph), 6.99 (br m, 11 H, Ph), 4.90 (s, 6 H, arene), 2.83 (m, 2 H, CH_2), 2.48 (m, 2 H, CH_2), 1.76 (m, 2 H, CH_2), 1.55 (m, 2 H, CH_2), −7.09 (dt, J_{PH} = 24 and 72 Hz, Mo−H); $^{31}P\{^1H\}$ NMR ($CDCl_2F$, 202 MHz, −125 °C) δ 99.9 (br s, 1 P, $-CH_2P(Ph)CH_2-$), 76.9, 69.8 (br s, 2 P, $-CH_2PPh_2$).

For **3D$^+$-d$_6$·F$_3$CSO$_3^-$**: ^1H NMR (CD_2Cl_2, 500 MHz, 20 °C) δ 7.42 (t, 6 H, J_{HH} = 6 Hz, Ph), 7.33 (t, 12 H, J_{HH} = 8 Hz, Ph), 7.05 (m, 12 H, Ph), 4.66 (q, 1.23 H, J_{PH} = 4 Hz, $C_6D_5H/C_6D_4H_2$), 1.85 (br s, 9 H, CH_3); ^2H NMR (CD_2Cl_2, 76.7 MHz, 20 °C) δ 4.74 (br s, 4.77 D, $C_6D_5H/C_6D_4H_2$), 0.06 (q, 1.00 D, J_{PD} = 11 Hz, Mo−D); $^{31}P\{^1H\}$ NMR (CD_2Cl_2, 202 MHz, 20 °C) δ 26.5 (t, J_{PD} = 11 Hz).

For **4H$^+$-d$_6$·F$_3$CSO$_3^-$** and **4D$^+$-d$_6$·F$_3$CSO$_3^-$**: ^1H NMR (CD_2Cl_2, 500 MHz, 20 °C) δ 7.43 (m, 9 H, Ph), 7.31 (m, 6 H, Ph), 4.36 (q, 0.91 H, J_{PH} = 4 Hz, $C_6D_5H/C_6D_4H_2$), 1.73 (br s, 18 H, CH_3), −1.26 (q, 0.24 H, J_{PH} = 75 Hz, Mo−H); ^2H NMR (CD_2Cl_2, 76.7 MHz, 20 °C) δ 4.36 (br s, 5.03 H, C_6D_6/C_6D_5H), −1.26 (q, 0.82 D, J_{PD} = 11 Hz, Mo-D); $^{31}P\{^1H\}$ NMR (CD_2Cl_2, 202 MHz, 20 °C) δ 11.6 (t, J_{PD} = 11 Hz, P−Mo-D), 11.5 (br s, P−Mo−H).

For **5H$^+$-d$_6$·F$_3$CSO$_3^-$** and **5D$^+$-d$_6$·F$_3$CSO$_3^-$**: ^1H NMR (CD_2Cl_2, 500 MHz, 20 °C) δ 4.63 (m, 0.87 H, $C_6D_5H/C_6D_4H_2$) 2.32 (s, 27 H, CH_3), −3.53 (q, 0.40 H, J_{PH} = 66 Hz, Mo−H); ^2H NMR (CD_2Cl_2, 76.7 MHz, 20 °C) δ 4.63 (m, 5.17 D, C_6D_6/C_6D_5H) −3.53 (q, 0.56 D, J_{PD} = 10 Hz, Mo-D); $^{31}P\{^1H\}$ NMR (CD_2Cl_2, 202 MHz, 20 °C) δ 0.8 (br s).

Kinetic Product Obtained from 1 and F_3CSO_3D at Low Temperature. A sample of **1** was added to an NMR tube equipped with a Schlenk adapter, and the tube was evacuated. The Freon $CDCl_2F$ was vacuum transferred into the tube, the solution was frozen with liquid N_2, and the tube was backfilled with N_2 gas. While still frozen, 1 equiv of F_3CSO_3D was added, the tube was evacuated, and it was flame-sealed. The frozen sample was transferred to an NMR probe that had been precooled to −150 °C. The probe was allowed to warm slowly. At −120 °C, the solution melted and a spectrum of **1** was obtained. At approximately −85 °C,[15] **1H$^+$-d$_1$** was obtained (no **1D$^+$-d$_1$**). No further change in the spectrum was observed as the sample was warmed to 25 °C.

Selective Spin Inversion Transfer (SSIT) Experiment. A sample of $\mathbf{1H^{\bullet+}PF_6^-}$ was added to an NMR tube equipped with a Schlenk adapter, and the tube was evacuated. The Freon $CDCl_2F$ was vacuum transferred into the tube, and it was flame-sealed. Because of the large difference in frequency between the arene and hydride resonances, the standard spin inversion transfer (SIT) pulse sequence[16−19] was impractical. An alternative pulse sequence was devised. Selective spin inversion transfer (SSIT) data were collected using the two-pulse sequence d_1, $2\pi/2$, τ_m, $\pi/2$, aq. The transmitter offset frequency was centered on the arene resonance. The relaxation delay d_1 was set equal to 5 times the longest T_1 to allow complete longitudinal relaxation between pulses. The 180° pulse was of sufficiently low power (and long duration) that surrounding resonances were unaffected. The mixing time τ_m was varied between 0.001 s and $5T_1$. A 90° pulse was applied at full power prior to FID acquisition. Data analysis for the SSIT pulse sequence is the same as the SIT pulse sequence.[20] A SSIT experiment at 25 °C indicated that no spin exchange takes place on the time scale of nuclear relaxation ($T_1 \approx$ 1 s).

Measurement of the Isomerization Rate of $\mathbf{1H^+}$. The ^{31}P NMR spectrum of $\mathbf{1H^+}$ exhibits C_s symmetry at −125 °C with a 2:1 ratio of phosphorus resonances at 43.2 and 34.5 ppm, respectively (vide supra). As the sample is heated, the two ^{31}P signals broaden and merge. At the coalescence temperature of −70 °C and $\Delta\delta$ of 202.36 Hz, the rate constant was determined using the equation for a two-site exchange with a 2:1 population:[21]

$$k_{203K} = \frac{2\pi\Delta\delta}{e^z + e^{-z}} \approx 3.01\Delta\delta = 5.3 \times 10^3\ s^{-1} \qquad (1)$$

$$z = \frac{1}{6}\ln\{3 + 2\sqrt{2}\} \qquad (2)$$

The corresponding activation barrier was estimated at the coalescence temperature:[22,23]

$$\Delta G^{\ddagger} = -RT_c[\ln(k/T_c) + \ln(h/K)] = 35\ kJ\ mol^{-1} \qquad (3)$$

where $R = 8.314$ J mol^{-1} K^{-1} is the gas constant, T_c is the coalescence temperature, $h = 6.626 \times 10^{-34}$ J s is Planck's constant, and $K = 1.381 \times 10^{-23}$ J K^{-1} is Boltzmann's constant.

General Procedure for Low-Temperature NMR Studies of $\mathbf{2_KH^+}$. A crystalline sample of **2** was placed as a solid in a N_2-purged NMR tube equipped with a Schlenk adapter. Solvent was added, and the resulting solution was frozen with liquid N_2. The acid solution was syringed (using a gastight Hamilton syringe) onto the frozen matrix under a positive N_2 gas flow, and then the valve was closed, vacuum was applied to the heterogeneous frozen mixture, and the tube was flame-sealed. The tube was transferred quickly from the liquid N_2 bath to a *n*-pentane/liquid N_2 slush bath at −100 °C for transport to the spectrometer. The probe of the spectrometer was precooled to −90 °C before insertion of the NMR tube.

Chart 2

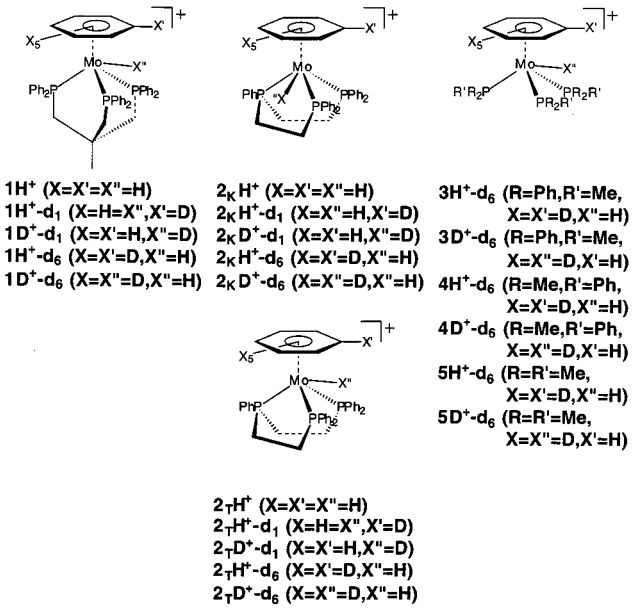

Chart 3

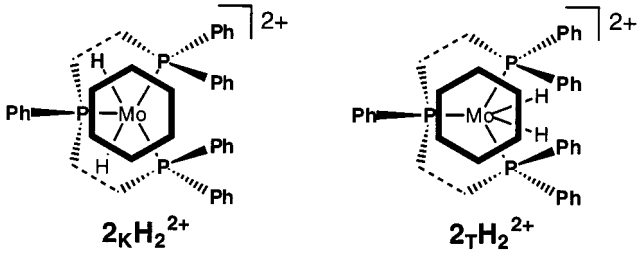

Measurement of the Epimerization Rate of $\mathbf{2_KH^+}$. The kinetic hydride $\mathbf{2_KH^+}$ was synthesized in situ at −90 °C in CD_2Cl_2 from **2** and F_3CSO_3H using the aforementioned process. The ^{31}P resonances that correspond to the terminal P donors of the TRIPHOS ligand of $\mathbf{2_KH^+}$ are nearly static at −97 °C (69.8 and 76.9 ppm). Under fast exchange conditions, the nuclei of the terminal P donors are rendered magnetically equivalent and the spectrum becomes consistent with overall C_s symmetry. At the coalescence temperature of −87 °C and $\Delta\delta$ of 202.36 Hz, the rate constant was determined using the standard equation:[24]

$$k_{186K} = 2\pi(\Delta\delta)/\sqrt{2} = 6.4 \times 10^3\ s^{-1} \qquad (4)$$

The corresponding activation barrier was estimated by eq 3 to be 31 kJ mol^{-1} at the coalescence temperature.

Measurement of the Isomerization Rate of $\mathbf{2_KH^+}$ to $\mathbf{2_TH^+}$. A solution of **2** (40 mM) and F_3CSO_3H (40 mM) was prepared at −90 °C using the aforementioned procedure. After the NMR sample was warmed to −60 °C in the spectrometer, three species are observed: the parent compound **2**, the kinetic monohydride $\mathbf{2_KH^+}$, the thermodynamic monohydride $\mathbf{2_TH^+}$, and small amounts of a kinetic dihydride of C_s symmetry, $\mathbf{2_KH_2^{2+}}$ (Charts 1−3). A thermodynamic dihydride $\mathbf{2_TH_2^{2+}}$ (Chart 3) that is observed at higher acid concentrations is not observed under these conditions. The distributions of these species as a function of time are illustrated in Figure 6. Given the fact that we have reacted an equimolar quantity of **2** and H^+, assuming the equilibrium between $\mathbf{2_KH^+}$ and $\mathbf{2_KH_2^{2+}}$ is

(15) It has been noted that CF_3SO_3H freezes very rapidly in CH_2Cl_2 at −95 °C and is not dissolved: Rothfuss, H.; Gusev, D. G.; Caulton, K. G. *Inorg. Chem.* **1995**, *34*, 2894. The protonation of **1** is probably very fast at low temperature, and warming to −85 °C is necessary to dissolve the acid.

(16) Bellon, S. F.; Chen, D.; Johnston, E. R. *J. Magn. Reson.* **1987**, *73*, 168.
(17) Alger, J. R.; Prestegard, J. H. *J. Magn. Reson.* **1977**, *27*, 137.
(18) Kuchel, R. W.; Chapman, B. E. *J. Theor. Biol.* **1983**, *105*, 569.
(19) Robinson, G.; Kuchel, P. W.; Chapman, B. E. *J. Magn. Reson.* **1985**, *63*, 314.
(20) Ashby, M. T.; Govindan, G. N.; Grafton, A. K. *J. Am. Chem. Soc.* **1994**, *116*, 4801.
(21) Shanan-Atidi, H.; Bar-Eli, K. H. *J. Phys. Chem.* **1970**, *74*, 961.
(22) Allerhand, A.; Gutowsky, H. S.; Jonas, J.; Meinzer, R. A. *J. Am. Chem. Soc.* **1966**, *88*, 5.
(23) Faller, J. W. *Adv. Organomet. Chem.* **1977**, *16*, 211−239.
(24) Green, M. L. H.; Wong, L.-L.; Sella, A. *Organometallics* **1992**, *11*, 2660.

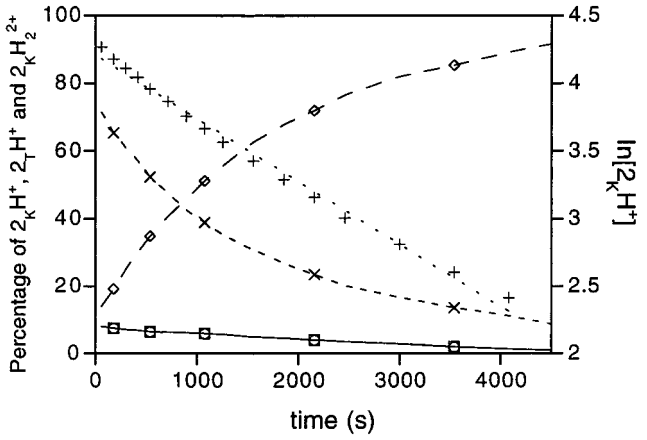

Figure 6. Distribution of **2** (○), $\mathbf{2_K}\mathbf{H}^+$ (×), $\mathbf{2_T}\mathbf{H}^+$ (◇), and $\mathbf{2_K}\mathbf{H_2}^{2+}$ (□) as a function of time when 1 equiv of H^+ is added to a 40 mmol solution of **2** in CD_2Cl_2 at −60 °C (left). The plot of ln[$\mathbf{2_K}\mathbf{H}^+$]/time (+) that was used to calculate the effective rate constant of $k_{obs} = 5.0 \times 10^{-4}$ s^{-1} for interconversion of $\mathbf{2_K}\mathbf{H}^+$ to $\mathbf{2_T}\mathbf{H}^+$ at −60 °C (right). All of the data for the plot on the right are illustrated, but only every fifth point is illustrated for the plots on the left.

rapid (as is suggested by the time dependence of the concentration curves), and the rate of formation of the product $\mathbf{2_T}\mathbf{H}^+$ depends only on the concentration of $\mathbf{2_K}\mathbf{H}^+$:

$$\mathbf{2} + \mathbf{2_K}\mathbf{H_2}^{2+} \underset{k_{-1}}{\overset{k_1}{\rightleftharpoons}} 2\ \mathbf{2_K}\mathbf{H}^+$$

$$\mathbf{2_K}\mathbf{H}^+ \xrightarrow{k_2} \mathbf{2_T}\mathbf{H}^+$$

The rate is given by[25]

$$\frac{d[\mathbf{2_T}\mathbf{H}^+]}{dt} = \frac{k_2\sqrt{K_1}}{2 + \sqrt{K_1}}[\mathbf{2_K}\mathbf{H}^+] \quad (5)$$

where the equilibrium constant K_1 may be determined by integration of the components at $t = 0$:

$$K_1 = \frac{[\mathbf{2_K}\mathbf{H}^+]^2}{[\mathbf{2}][\mathbf{2_K}\mathbf{H_2}^{2+}]} = 77 \quad (6)$$

From the data of Figure 6, $k_{obs} = 5.0 \times 10^{-4}$ s^{-1}, yielding $k_2 = 6.1 \times 10^{-4}$ s^{-1}, which gives an activation barrier of $\Delta G^{\ddagger} = 65$ kJ mol^{-1} at −60 °C.

Tracer Studies Involving 1−5. All of the tracer experiments that are summarized in Table 3 were carried out at room temperature (22 °C). Each experiment was carried out twice, once in CD_2Cl_2 (to obtain ^{1}H NMR spectra) and once in CH_2Cl_2 (to obtain ^{2}H NMR spectra). Solutions of the d_6 derivatives of **1**−**5** (ca. 100 mM) were transferred to NMR tubes in a glovebox. Approximately 1 equiv of F_3CSO_3H was added via a microliter syringe to the NMR tube, the tube was flame-sealed, and the NMR spectra were collected. NMR spectra collected the following day revealed no significant changes.

Electronic Structure and Geometry Calculations. The molecular mechanics and molecular orbital calculations on **1**−**5** were performed with SPARTAN 5.0.[26] The geometries of **1**−**5** were optimized using the Merck molecular force field (MMFF), then refined using the semiempirical method PM3(tm). In

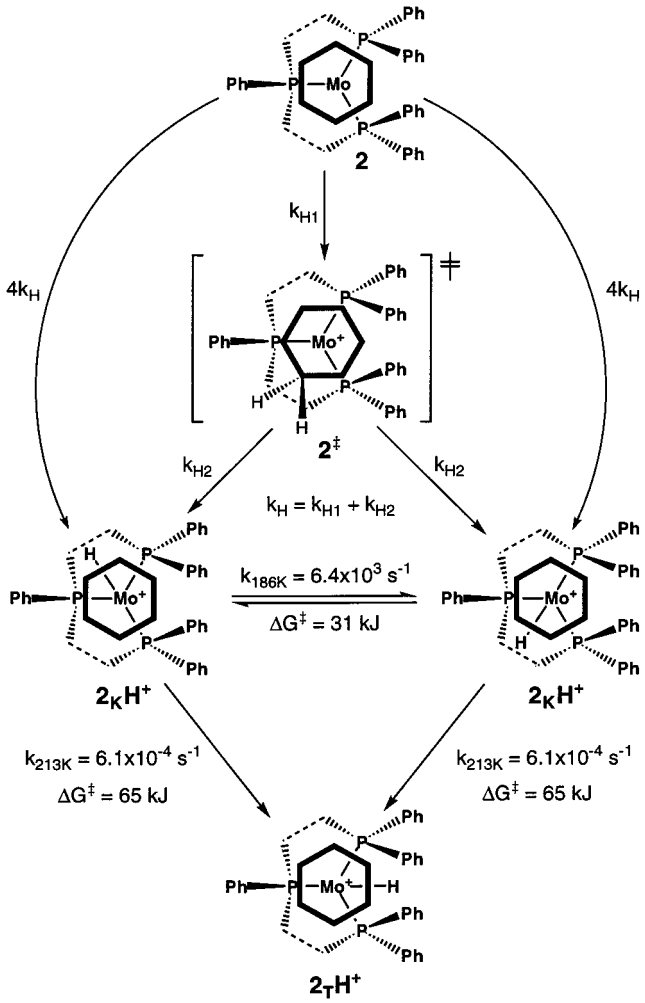

Figure 7. Proposed reaction pathways for the interconversion of **2**, $\mathbf{2_K}\mathbf{H}^+$, and $\mathbf{2_T}\mathbf{H}^+$. The rate constant for epimerization of $\mathbf{2_K}\mathbf{H}^+$ was measured at the coalescence temperature of −87 °C to be $k = 6.4 \times 10^3$ s^{-1} ($\Delta G^{\ddagger} \cong 31$ kJ mol^{-1}). The rate constant for isomerization of $\mathbf{2_K}\mathbf{H}^+$ to $\mathbf{2_T}\mathbf{H}^+$ was determined to be $k = 6.1 \times 10^{-4}$ s^{-1} ($\Delta G^{\ddagger} \cong 65$ kJ mol^{-1}) at −60 °C.

Table 2, the computed geometries are compared with the metric data for **1**−**4** that were determined by X-ray crystallography. The computed geometry of **5** is also given in Table 2. The CPK models of Figure 8 may be compared with the thermal ellipsoid figures for **1**−**4** in Figures 1−4. Figure 8 also illustrates surface electron density plots of the (η^6-C_6H_6)Mo(P)$_3$ derivatives **1**−**5** onto which is mapped the surface electron density of the three highest occupied molecular orbitals (the metal t_{2g}-type orbitals) as calculated using the PM3(tm) method. The isodensity surfaces (0.002 e/au^3) have been chosen to reflect van der Waals radii. The colors range from red (no frontier orbital character) to blue (5×10^{-5} e/au^3 frontier orbital character). For some derivatives, especially **4**, several stationary-state comformers of similar energies were encountered. The ones illustrated in Figure 8 most closely resemble the conformations that were observed in the solid state. All of the computed stationary-state conformers gave mapped surface electron density plots that were comparable (with respect to penetrating metal density) to those that are illustrated in Figure 8. Electron structure calculations that were performed on **1**−**4** using the coordinates that were determined by X-ray crystallography also gave mapped surface electron density plots that were comparable to those of Figure 8.

X-ray Crystallography. The conditions that were used to collect X-ray data for **1**−**4** are summarized in Table 1. The

(25) Schmid, R.; Sapunov, V. N. *Non-formal Kinetics*; Verlag Chemie: Weinheim, 1982.

(26) *Spartan*, version 5.0; Wavefunction, Inc.: 18401 Von Karman Avenue, Suite 370, Irvine, CA 92612.

Table 1. Crystal Data for Compounds 1−4

	1	2	3	4
formula	$C_{47}H_{45}MoP_3$	$C_{40}H_{39}MoP_3$	$C_{45}H_{45}MoP_3$	$C_{30}H_{39}MoP_3$
fw	798.68	708.56	774.66	588.46
space group	$P2_1/n$	$P2_1/n$	$R3$	$P2_1/n$
cryst syst	monoclinic	monoclinic	rhombohedral	monoclinic
a, Å	9.636(4)	9.1830(10)	10.7703(5)	9.4393(8)
b, Å	20.277(5)	17.385(2)		9.4066(9)
c, Å	19.670(3)	21.413(3)		32.346(4)
α, deg	90	90	110.241(3)	90
β, deg	93.05(2)	101.830(10)		95.518(7)
γ, deg	90	90		90
V, Å^3	3838(2)	3345.9(7)	933.33(8)	2858.7(5)
T, K	203(2)	188(2)	173(2)	173(2)
Z	4	4	1	4
D_{calc}, g cm^{-3}	1.382	1.407	1.378	1.367
μ, mm^{-1}	0.500	0.564	0.512	0.644
final R indices[a]	R1 = 0.0379	R1 = 0.0451	R1 = 0.0224	R1 = 0.0297
[$I > 2\sigma(I)$]	wR2 = 0.0910	wR2 = 0.1095	wR2 = 0.0587	wR2 =0.0730
R indices [all data	R1 = 0.0594	R1 = 0.0614	R1 = 0.0225	R1 = 0.0369
used in refinement]	wR2 = 0.1147	wR2 = 0.1206	wR2 = 0.0595	wR2 = 0.0788
GOF	1.095	1.045	1.045	1.054

[a] $R1 = \sum|F_o| - |F_c||/\sum|F_o|$; $wR2 = [\sum[w(F_o^2 - F_c^2)]/\sum[w(F_o^2)^2]]^{1/2}$; $w = 1/\sum[\sigma^2(F_o)^2 + (aP)^2 + (bP)^2 + (cP)^2]$, $P = (F_o)^2[1/3 + [2*(F_o)^2/3]]$ for $F_o^2 \geq 0$ (otherwise zero). $GOF = [\sum[w(F_o^2 - F_c^2)]/(n - m)]^{1/2}$, where n = no. of reflections observed and m = no. of parameters.

Table 2. Selected Interatomic Distances (Å) and Angles (deg) Determined by X-ray Diffraction (Compounds 1−4) and Computationally Using the PM3(tm) Method (Compounds 1−5)

	(η^6-C_6H_6)Mo(TRIPOD) 1		(η^6-C_6H_6)Mo(TRIPHOS) 2		(η^6-C_6H_6)Mo(PPh_2Me)$_3$ 3		(η^6-C_6H_6)Mo($PPhMe_2$)$_3$ 4		(η^6-C_6H_6)Mo(PMe_3)$_3$ 5
	XRD C_1	PM3(tm) C_3	XRD C_1	PM3(tm) C_1	XRD C_3	PM3(tm) C_3	XRD C_1	PM3(tm) C_3	PM3(tm) C_3
Mo−P1	2.412(1)	2.389	2.3687(8)	2.400	2.4438(5)	2.407	2.4431(7)	2.389	2.386
Mo−P2	2.3866(9)		2.4045(8)	2.383			2.4431(6)		
Mo−P3	2.3843(9)		2.3926(8)	2.369			2.4428(7)		
Mo−Bz_{cent}[a]	1.816(3)	1.883	1.789(4)	1.886	1.788(2)	1.903	1.781(3)	1.886	1.878
P1−Mo−P2	84.81(3)	85.76	78.91(3)	79.11	92.37(2)	93.44	92.32(2)	93.97	93.30
P1−Mo−P3	83.50(3)		79.80(3)	79.16			92.25(2)		
P2−Mo−P3	83.13(3)		92.74(3)	99.05			90.49(2)		
Bz_{cent}−Mo−P1	129.2(1)	128.21	131.8(1)	133.66	123.6(1)	122.79	123.6(1)	122.43	122.90
Bz_{cent}−Mo−P2	128.4(1)		132.3(1)	128.01			123.6(1)		
Bz_{cent}−Mo−P3	131.0(1)		124.0(1)	122.75			124.9(1)		

[a] Bz_{cent} is the centroid of a η^6-arene ligand.

X-ray data for **1** were collected with an Enraf-Nonius CAD-4 diffractometer, and the data for **2**−**4** were collected on a Siemens P4 diffractometer. Monochromated Mo Kα radiation (λ = 0.710 73 Å) was employed. The data were corrected for Lorentz and polarization effects. An empirical absorption correction based on ψ scans was applied to **2**−**4**. All of the structures were determined and refined using the SHELXTL (Siemens) system. The structures of **1** and **2** were solved by direct methods. The structures of **3** and **4** were solved by the heavy atom method. All structures were refined by full-matrix least-squares on F^2 using all reflections. All of the hydrogen atoms were included in the refinements with idealized parameters. For all the hydrogen atoms except the methyl atoms, the temperature factors were assigned to be 1.2 times the U(eq) value of the carbon atom on which they ride; for the methyl hydrogens the values were 1.5 times that of the U(eq) values of the corresponding carbon atoms. For **2**, two conformations of the TRIPHOS ligand are observed, which were modeled by large thermal parameters for C(37) and C(38) and two occupation sites (50:50) for the arene rings C7−C12 (C7A−C12A) and C19−C24 (C19A−C24A). Only one conformation is depicted in Figure 2. A figure that depicts both conformations is available in the Supporting Information. For **3**, best refinement was achieved in the noncentric space group $R3$ as a racemic twin with a final BASF parameter of 0.26(2), suggesting a 26:74 mixture. Other details concerning the structure refinements are summarized in Table 1. Selected metric data for **1**−**4** are compared in Table 2. Tables of atomic coordinates and equivalent isotropic displacement parameters, anisotropic displacement parameters, hydrogen coordinates and isotropic parameters, and bond lengths and angles are available as Supporting Information.

Results

Synthesis and Solution Properties of 1−5. Complex **1** (Chart 1) is most effectively synthesized in a melt reaction containing (η^6-C_6H_6)$_2$Mo and TRIPOD. However, the derivatives **2**−**5** are more readily synthesized if a solvent is employed. Compounds **1**−**5** and their isotopomers were characterized by NMR and mass spectrometry and, in the case of new compounds, by combustion analysis. ^{1}H, ^{2}H (when appropriate), and ^{31}P NMR were measured. It is noteworthy that signals for the ^{1}H (and ^{2}H for isotopomers) nuclei of the arene ligands and the ^{31}P nuclei were very broad (and sometimes not observed) for **1** and **3**−**5** in dichloromethane solvent, though the ^{1}H resonances of the rest of the phosphine ligands were observed. The observed resonances exhibited expected chemical shifts. In contrast, benzene solutions of the same samples exhibited all of the expected resonances. We believe this peculiar solvent effect is due to trace paramagnetic impurities that

are soluble in dichloromethane but not soluble in benzene. We have previously characterized the paramagnetic one-electron-oxidation product of **1**,[10] and we suspect the likely impurity is $[(\eta^6\text{-}C_6H_6)Mo(P)_3]^+$. Self-exchange between $(\eta^6\text{-}C_6H_6)Mo(P)_3$ and $[(\eta^6\text{-}C_6H_6)Mo(P)_3]^+$ could give rise to broadened resonances, especially in the first coordination sphere of the metal center.[27] We have noted on occasion that small amounts of a yellow precipitate (the color of $\mathbf{1}^+$) forms when benzene solutions of **1** are allowed to stand, even under an inert atmosphere. Since the solutions were prepared from crystalline samples with particular attention to exclusion of moisture and oxygen, the paramagnetic impurity may be the result of partial oxidation by the solvent or some type of disproportionation. A similar problem was observed in other polar solvents such as THF. Interestingly, we encountered no problem obtaining complete NMR spectra of **2** in dichloromethane. To minimize formation of the impurity, dichloromethane solutions of **1**−**5** were prepared fresh and used immediately for the studies that are described herein. It is noteworthy that the corresponding protonated species $\mathbf{1H}^+$−$\mathbf{5H}^+$ do not exhibit stability problems in dichloromethane, and all of their NMR resonances were observed. This is consistent with the expected greater stabilities of the protonated species with respect to oxidation.

Molecular Structures of 1−4. Since rationalization of the regiochemistry of protonation will depend on an understanding of the molecular structures of **1**−**5** (vide infra), crystal structures of **1**−**4** were determined by X-ray crystallography. Efforts to obtain diffraction quality crystals of **5** failed. The crystal structure parameters for **1**−**4** are summarized in Table 1. The molecular structures of **1**−**4** are compared in Table 2. Thermal ellipsoid drawings of **1**−**4** and the labeling schemes are presented in Figures 1−4. Other crystallographic information is available in the Supporting Information. Compound **3** exhibits crystallographically imposed C_3 symmetry, whereas **1** and **4** are approximately C_3 symmetric. The molecular structure of **2** has no crystallographic symmetry, although small conformational changes reveal its C_s molecular symmetry. The unremarkable metric data of Table 2 compare to that previously reported for other $(\eta^6$-arene$)Mo(P)_3$ complexes such as $(\eta^6\text{-}C_6H_5(PPhMe))Mo(PPh_2Me)_3$,[28] $[(\mu^2\text{-}\eta^6\text{-}C_6H_5(PMe_2))Mo(PPhMe_2)_2]_2$,[29] and $(\eta^6\text{-}C_6H_5(PPhMe))Mo(PPh_2Me)(Ph_2PCH(Me)CH_2PPh_2)$.[30] The molecular structures of **1**−**5** that were computed using the PM3(tm) method are compared in Table 2 with those that were determined by X-ray crystallography for **1**−**4**. Figure 8 (left) depicts the computed structures of **1**−**5** as space-filled models. Of particular interest with respect to the present study are the conformations observed for **1**−**5** (vide infra). The computed conformations (Figure 8, left) resemble the experimental conformations (Figures 1−4).

Electronic Structures of 1−5. We have recently reported a detailed combined theoretical and experi-

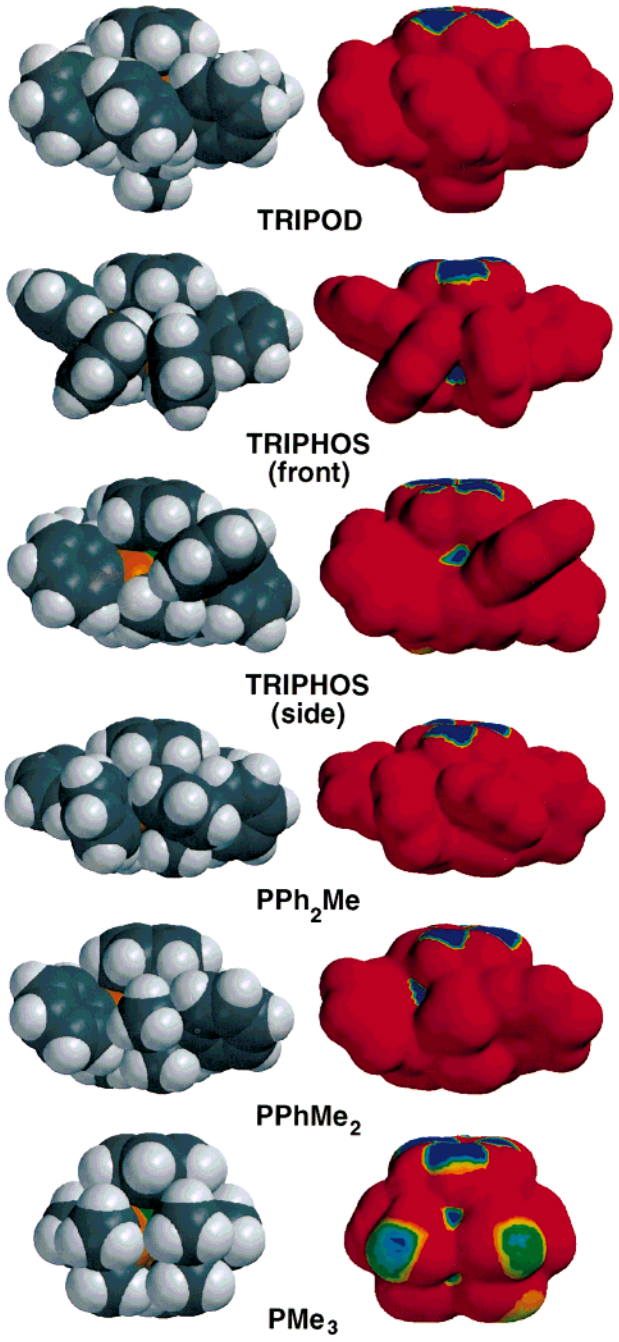

Figure 8. CPK models (left) and surface electron density plots (right) of $(\eta^6\text{-}C_6H_6)Mo(P)_3$: **1** ($(P)_3$ = TRIPOD), **2** ($(P)_3$ = TRIPHOS), **3** (P = PPh_2Me), **4** (P = $PPhMe_2$), and **5** (P = PMe_3). The isodensity surfaces (0.002 e/au^3) of the electron density plots have been chosen to reflect the van der Waals radii of the CPK models. The surface electron density of the three highest occupied molecular orbitals (the metal t_{2g}-type orbitals) as calculated using the PM3(tm) method have been mapped onto the isodensity surfaces. The colors range from red (no frontier orbital character) to blue (5×10^{-5} e/au^3 frontier orbital character). The geometries are optimized by the PM3(tm) method (although similar figures are obtained using the crystal structures of **1**−**4**). Note that two perspectives of **2** are presented. The CPK view from the "side" suggests the metal center is sterically accessible, and the electron density plot shows metal density is available at the surface. The view from the "front" demonstrates available surface metal density, but high steric congestion.

(27) Bertini, I.; Luchinat, C. In *Physical Methods for Chemists*; Drago, R. S., Ed.; Saunders College Publishing: Ft. Worth, TX, 1992; pp 500−552.
(28) Mason, R.; Thomas, K. M.; Heath, G. A. *J. Organomet. Chem.* **1975**, *90*, 195.
(29) Cotton, F. A.; Luck, R. L.; Morris, R. H. *Organometallics* **1989**, *8*, 1282.
(30) Morris, R. H.; Sawyer, J. F.; Sella, A. *Acta Crystallogr., Sect. C* **1988**, *44*, 23.

mental investigation of the electronic structures of **1** and $\mathbf{1}^+$. We concluded that the three highest occupied frontier orbitals are largely metal in character (the t_{2g}-type orbitals) and very close in energy. In fact, various computational methods (semiempirical, ab initio HF and DFT) predict different ordering of these orbitals depending on the model and the basis set employed. However, all of the computational methods agree the three orbitals are close in energy and that two of the three frontier orbitals are largely metal in character, but two bear significant η^6-arene character. Figure 8 (right) illustrates the three highest occupied frontier orbitals of **1**−**5** (HOMO, HOMO-1, and HOMO-2) mapped onto plots of total electron density using computed geometries. Thus, Figure 8 (right) illustrates the sterically accessible metal electron density. Importantly, very similar plots were obtained when the crystal structures of **1**−**4** were employed in the calculation, albeit with different isodensity surface parameters to account for the shorter metal−ligand distances that are observed experimentally as compared to the computed distances (Table 2). Also, very similar plots for **1** (i.e., no surface-accessible metal density) were observed for PM3(tm), HF6-31G*, and DFT-BP* calculations.[10] Since the qualitative nature of Figure 8 (left) does not appear to be sensitive to interatomic distances, the conformations that are predicted using PM3(tm), HF, MP2, and DFT are comparable, and we only intend to discuss the qualitative features of Figure 8; we only discuss the results of the PM3(tm) calculations here.

Tracer Studies Involving Protonation of 1. Treatment of **1** with 1 equiv of F_3CSO_3D in dichloromethane gave $\mathbf{1H^+\text{-}d_1}$ (Chart 2). The PF_6^- salt of $\mathbf{1H^+\text{-}d_1}$ was characterized by ^1H, ^2H, and ^{31}P NMR spectroscopy and, after deprotonation with NaOMe, by DIP and FAB MS. The NMR data reveal the presence of a Mo−H (not a Mo−D) bond. The parent peaks of the deprotonated product $\mathbf{1\text{-}d_1}$ were one *m*/*z* unit higher than those of the undeuterated compound. The latter experiment suggests that the arene ligand is involved in the protonation of the metal center, but it does not demonstrate that the hydride ligand originates from the arene, for it could originate from another source of protium, e.g., from the solvent. Also, as discussed above, a curious feature of the various (η^6-arene)Mo(P)$_3$ derivatives is that the arene resonances are extremely broad in dichloromethane (the solvent employed for the protonation reactions), making accurate integration difficult. Addressing the concern that the D^+ tracer may undergo exchange with adventitious sources of H^+ (e.g., moisture) before reacting with the metal complex, a complementary experiment was performed. The perdeuterioarene derivative $\mathbf{1\text{-}d_6}$, which was synthesized from $(\eta^6\text{-}C_6D_6)_2Mo$, was treated with 1 equiv of F_3CSO_3H in dichloromethane to yield $[(\eta^6\text{-}C_6D_5H)Mo(TRIPOD)D]^+$, $\mathbf{1H^+\text{-}d_6}$. The PF_6 salt of $\mathbf{1H^+\text{-}d_6}$ was characterized by ^1H, ^2H, and ^{31}P NMR spectroscopy and, after deprotonation with NaOMe to give $\mathbf{1\text{-}d_5}$, by DIP and FAB MS. The protonation experiment employing $\mathbf{1\text{-}d_6}$ demonstrates that the hydride ligand originates from the arene ligand.

Spin-Labeling NMR Experiments To Rule Out Alternative Mechanisms. While the origin of the hydride ligand is demonstrated by the tracer studies, these experiments do not unambiguously demonstrate that the initial attack is *exo*. Referring to Figure 5, *exo* addition would correspond to $\mathbf{1 \rightarrow 1^{\ddagger}\text{-}d_1 \rightarrow 1H^+\text{-}d_1}$. If the hydride ligand exchanges rapidly with the hydrogens of the arene ligand ($\mathbf{1D^+\text{-}d_1 \rightleftharpoons 1^{\ddagger}\text{-}d_1' \rightleftharpoons 1^{\ddagger}\text{-}d_1'' \rightleftharpoons 1H^+\text{-}d_1}$) and one ignores isotope effects, statistics dictate a 1:6 ratio of $\mathbf{1D^+\text{-}d_1}$:$\mathbf{1H^+\text{-}d_1}$. Thus, the initial intermolecular attack could be at the metal ($\mathbf{1 \rightarrow 1D^+\text{-}d_1}$), followed by intramolecular *endo* protonation of the arene ($\mathbf{1D^+\text{-}d_1 \rightarrow 1^{\ddagger}\text{-}d_1'}$), a hydrogen shift ($\mathbf{1^{\ddagger}\text{-}d_1' \rightarrow 1^{\ddagger}\text{-}d_1''}$), and finally transfer of the *endo* proton to the metal ($\mathbf{1^{\ddagger}\text{-}d_1'' \rightarrow 1H^+\text{-}d_1}$). Although it is problematic to differentiate between these two pathways with the tracer experiments, we have qualitative kinetic information that rules out the $\mathbf{1 \rightarrow 1D^+\text{-}d_1 \rightarrow 1^{\ddagger}\text{-}d_1' \rightarrow 1^{\ddagger}\text{-}d_1'' \rightarrow 1H^+\text{-}d_1}$ pathway. We have prepared equimolar solutions of **1** and F_3CSO_3D at −150 °C in $CDCl_2F$ and found protonation does not occur until the solution is warmed to ca. −85 °C.[15] The first product that is observed in these experiments is $\mathbf{1H^+\text{-}d_1}$. Selective spin inversion transfer (SSIT) NMR experiments at 25 °C indicate that no spin exchange takes place between the arene ligand hydrogens and the metal hydride on the time scale of nuclear relaxation ($T_1 \approx 1$ s). Extrapolating to −85 °C, the rate of formation of $\mathbf{1H^+\text{-}d_1}$ must be much faster than the rate of intramolecular chemical exchange ($\mathbf{1D^+\text{-}d_1 \rightleftharpoons 1^{\ddagger}\text{-}d_1' \rightleftharpoons 1^{\ddagger}\text{-}d_1'' \rightleftharpoons 1H^+\text{-}d_1}$).

Comparative Regiochemistry of Protonation of 1−5. When **1**−**5** were reacted with D^+, we obtained evidence in some cases that the isotope tracer was exchanging with adventitious sources of H^+ (probably in the form of moisture) before reacting with the metal complexes. In such cases mass balance was poor and not all of the deuterium tracer was accounted for in the metal−hydride complexes. To avoid this problem, all of the tracer studies we report herein involve reaction of the η^6-C_6D_6 derivatives of **1**−**5** with H^+. These experiments were performed at least twice, once in CD_2Cl_2 so ^1H NMR could be run, and once in CH_2Cl_2, so ^2H NMR could be run. In some cases (especially **1** and **2**) the experiments were repeated dozens of times using the same or slightly different conditions (i.e., different solvents, concentrations, and temperatures) to ensure reproducibility and generality of the conclusions herein. In the case of **1**, direct protonation of the metal center was never indicated. For **2**, attack at the arene ligand and the metal was always observed with partitioning of ca. 4:1.

Discussion

Electrophilic Aromatic Substitution of Arene Ligands. Complexation of arenes has a marked effect on their reaction properties.[31,32] Since the metal is net electron withdrawing, binding arenes to metals has the effect of activating them toward nucleophilic attack while deactivating them with respect to electrophilic attack. We are aware of only three types of electrophilic aromatic substitution reactions that occur with metal-bound arenes: (1) protonation, (2) Friedel−Crafts acetylation,[33−38] and (3) addition of iminium salts.[39]

(31) Silverthorn, W. E. *Adv. Organomet. Chem.* **1975**, *13*, 47−137.
(32) Hegedus, L. S. *Transition Metals in the Synthesis of Complex Organic Molecules*; University Science Books: Mill Valley, CA, 1994.
(33) Riemschneider, R.; Becker, O.; Franz, K. *Monatsch. Chem.* **1959**, *90*, 571.

While there are many examples of the first two types of reactions, only one example of addition of iminium salts has been reported, the reaction of $[(\eta^4\text{-}C_6H_6)Mn(CO)_3]^-$ with $[R_2C{=}NR_2]^+$ to give $(\eta^5\text{-}C_6H_6CR_2NR_2)Mn(CO)_3$.[39] In this case the metal is anionic, the arene ligand is bound η^4, and the electrophile is cationic, which are factors that are undoubtedly important. Other electrophiles (besides of course protons) apparently do not react with $[(\eta^4\text{-}C_6H_6)Mn(CO)_3]^-$.[40] We have made similar observations for **1**. Indeed, **1** reacts with $[CH_2{=}NMe_2]I$ (Eschenmoser's salt) to give $[(\eta^6\text{-}C_6H_5(CH_2NMe_2))Mo(TRIPOD)(H)]I$,[41] which has been characterized in situ by its distinctive NMR spectrum; however, the product has proven difficult to isolate. Compound **1** does not react with other electrophiles such as Et_3OBF_4 and F_3CSO_3Me. Instead, hydrolysis products from the electrophiles simply protonate **1** to give $\mathbf{1H}^+$. Alkyl halides do react with **1** under neat conditions at elevated temperatures in the absence of Lewis acid catalysts to give mixtures of $\mathbf{1H}^+$ and $[(\eta^6\text{-}C_6H_5R)Mo(TRIPOD)(H)]^+$.[41] We suspect these reactions are the result of initial single electron transfer (SET). Interestingly, we were unable to achieve Friedel−Crafts acetylation of **1** with $CH_3COCl/AlCl_3$. Protonation, it would seem, is the only clean electrophilic reaction that occurs for **1** and other $(\eta^6\text{-arene})Mo(P)_3$ complexes. Before turning our attention to the mechanism of protonation of these complexes, we will first discuss the protonation of η^6-arene complexes and make a distinction between such reactions and those for η^2- and η^4-arene complexes.

Protonation of η^6-Arene Metal Complexes. Protonation reactions of η^6-arene metal complexes were first studied by Wilkinson et al. in 1962.[42] In that study a series of arene−Cr complexes in a $BF_3{\cdot}H_2O/CF_3COOH$ mixture were shown to have protonated metal centers characterized by high-field ^{1}H NMR resonances. In the intervening years, derivatives of $(\eta^6\text{-arene})Cr(CO)_3$ have been thoroughly studied due in part to the ease of their syntheses.[43−49] Particularly relevant to the present study is an investigation by McGlinchey et al. of the protonation of $(\eta^6\text{-}C_6Et_6)M(CO)_3$ (M = Cr and W) using ^{13}C NMR and computational methods.[50] In contrast to Olah's work, McGlinchey has suggested that the protonated metal centers of $[(\eta^6\text{-}C_6Et_6)M(CO)_3(H)]^+$ exhibit an unprecedented static C_{3v} geometry with the hydride ligands oriented along the symmetry axis, enforced by the steric demands of the arene ligand. Molecular orbital calculations at various levels suggest such a geometry is disfavored electronically.[10,50] Furthermore, their argument is based upon the simplicity of NMR spectra seen at low temperature, but we have observed dynamic spectra for $\mathbf{1H}^+$ under similar conditions. Finally, it should be pointed out that phosphine ligands are more basic and poorer π-acceptors than carbonyls;[10] therefore, substitution of one or more of the carbonyl ligands of $(\eta^6\text{-arene})M(CO)_3$ with phosphine ligands can produce highly electron-rich metal complexes that are readily protonated.[14,51−55] However, phosphine substitution does not have a marked effect on the ordering or character of the frontier orbitals of three-legged piano-stool complexes.[10]

Protonation of η^2- and η^4-Arene Metal Complexes. Electrophilic reactions with arene complexes which are η^2 and η^4 bound are also known. Cooper et al. have protonated $[(\eta^4\text{-}C_6H_6)Cr(CO)_3]^{2-}$ and $[(\eta^4\text{-}C_6H_6)Mn(CO)_3]^-$ complexes to form cyclohexadienyl species, and in the former case protonation was shown to be metal mediated (i.e., protonation of the metal followed by proton transfer to the *endo* face of the arene, precisely the opposite mechanism compared to that observed for **1**).[56,57] This example clearly illustrates the significance of steric and electronic factors (vide infra). Dihaptocoordinated aromatic hydrocarbons have been protonated to form the cyclohexadienyl cations.[58] In a recent study, Harman et al. have protonated $[Os(NH_3)_5(\eta^2\text{-arene})](OTf)_2$ to form the $[Os(NH_3)_5(\eta^3\text{-areneH})](OTf)_3$ complexes in which areneH is an η^3-bound cyclohexadienyl ligand.[59] Given the electron-withdrawing nature of the metal, it seems likely that electrophilic attack on η^2- and η^4-arene metal complexes takes place at the uncoordinated double bond(s).

Stereoelectronic Factors That Govern the Site of Attack by H^+ on 1−5. Protonation of **1**−**5** in aprotic, nonpolar media such as dichloromethane presumably involves delivery of H^+ as a tight ion pair with its conjugate base (X^-). It is reasonable to expect that the nature of the base might influence the mechanism. Thus, a strong base would involve less polarization of the H−X bond and a bulky X^- group might discourage direct attack by HX on the metal center. While these issues may be important in determining selectivity, the

(34) Ercoli, R.; Calderazzo, F.; Mantica, E. *Chim. Ind. (Milan)* **1959**, *41*, 404.
(35) Gracey, D. E. F.; Jackson, W. R.; Jennings, W. R. *J. Chem. Soc., Chem. Commun.* **1968**, 366.
(36) Herberich, G. E.; Fischer, E. O. *Chem. Ber.* **1962**, *95*, 2803.
(37) Jackson, W. R.; Jennings, W. B. *J. Chem. Soc., Chem. Commun.* **1966**, 824.
(38) Jackson, W. R.; Jennings, W. B. *J. Chem. Soc. B* **1969**, 1221.
(39) Park, S.-H. K.; Geib, S. J.; Cooper, N. J. *J. Am. Chem. Soc.* **1997**, *119*, 8365.
(40) Thompson, R. L. Ph.D. Thesis, University of Pittsburgh, 1993.
(41) Asirvatham, V. S.; Ashby, M. T. Unpublished results.
(42) Davison, A.; McFarlane, W.; Pratt, L.; Wilkinson, G. *J. Chem. Soc.* **1962**, 3653.
(43) Olah, G. A.; Yu, S. H. *J. Org. Chem.* **1976**, *41*, 717.
(44) Kursanov, D. N.; Setkina, V. N.; Petrovskii, P. V.; Zdanovich, V. I.; Baranetskaya, N. K.; Rubin, I. D. *J. Organomet. Chem.* **1972**, *37*, 339.
(45) Setkina, V. N.; Baranetskaya, N. K.; Ginzburg, A. G.; Zdanovich, V. I.; Nefedova, M. N.; Kursanov, D. N. *J. Organomet. Chem.* **1973**, *61*, 287.
(46) Losilkina, V. I.; Petrovskii, P. V.; Baranetskaya, N. K.; Setkina, V. N. *Bull. Acad. Sci. USSR, Div. Chem. Sci.* **1984**, *33*, 723.
(47) Rosca, S.; Chiraleu, F.; Rosca, S. I. *Rev. Roumaine Chim.* **1991**, *36*, 693.
(48) Losilkina, V. I.; Estekhina, M. N.; Baranetskaya, N. K.; Setkina, V. N. *J. Organomet. Chem.* **1986**, *299*, 187.
(49) Lillya, C. P.; Sahatjian, R. A. *Inorg. Chem.* **1972**, *11*, 889.
(50) Mailvaganam, B.; Sayer, B. G.; McGlinchey, M. J. *Organometallics* **1990**, *9*, 1089.
(51) Green, M. L. H.; Mitchard, L. C.; Silverthorn, W. E. *J. Chem. Soc. A* **1971**, 2929.
(52) Green, M. L. H.; Mitchard, L. C.; Silverthorn, W. E. *J. Chem. Soc., Dalton Trans.* **1974**, 1361.
(53) Green, M. L. H.; Hughes, A. K.; Lincoln, P.; Martin-Polo, J. J.; Mountford, P.; Sella, A.; Wong, L.; Bandy, J. A.; Banks, T. W.; Prout, K.; Watkin, D. J. *J. Chem. Soc., Dalton Trans.* **1992**, 2063.
(54) Losilkina, V. I.; Petrovskii, P. V.; Baranetskaya, N. K.; Setkina, V. N.; Kursanov, D. N. *Bull. Acad. Sci. USSR, Div. Chem. Sci.* **1983**, *32*, 2537.
(55) Losilkina, V. I.; Baranetskaya, N. K.; Tolkunova, V. S.; Krylova, A. I.; Vil'chevskaya, V. D.; Setkina, V. N. *J. Gen. Chem. USSR (Engl. Transl.)* **1987**, *57*, 753.
(56) Leong, V. S.; Cooper, N. J. *J. Am. Chem. Soc.* **1988**, *110*, 2644.
(57) Thompson, R. L.; Lee, S.; Rheingold, A. L.; Cooper, N. J. *Organometallics* **1991**, *10*, 1657.
(58) Winemiller, M. D.; Kopach, M. E.; Harman, W. D. *J. Am. Chem. Soc.* **1997**, *119*, 2096.
(59) Winemiller, M. D.; Kelsch, B. A.; Sabat, M.; Harman, W. D. *Organometallics* **1997**, *16*, 3672.

Table 3. Partitioning of Metal versus Arene Attack by H^+ on (η^6-C_6D_6)Mo(P)$_3$ upon Reaction with 1 equiv of F_3CSO_3H at 22 °C As Measured by ^1H and ^2H NMR[a]

	^{1}H NMR		^{2}H NMR	
cmpd, ligand	metal attack (%)	arene attack (%)	metal attack (%)	arene attack (%)
1, TRIPOD	0	100	0	100
2, TRIPHOS	88	12	72	28
3, $(PPh_2Me)_3$	0	100	0	100
4, $(PPhMe_2)_3$	22	78	16	84
5, $(PMe_3)_3$	37	63	39	61

[a] Note: these results were obtained from separate experiments in CD_2Cl_2 for the ^{1}H NMR and CH_2Cl_2 for the ^{2}H NMR. The percentages are derived from integrations of the arene and hydride ligand resonances taking into account the ratio of the C_6D_6/C_6D_5H isotopomers that were reacted with H^+. It is assumed that H^+ attack on the C_6D_5H isotopomer takes place without a KIE (i.e., D^+ will be transferred to the metal 5/6 of the time and H^+ will be transferred 1/6 of the time).

purpose of this study has been to explore the influence of the ancillary ligands. Furthermore, we have obtained very similar results for the tracer studies when F_3CSO_3H, F_3CCO_2H, HPF_6 (aq), HBF_4·(OEt_2), and HCl (aq) are employed.

Our recent study of the electronic structures of **1** and $\mathbf{1}^+$ illustrated that two of the three filled metal-based frontier orbitals have substantial arene character.[10] Thus, while protonation of the metal center is thermodynamically preferred, an incoming electrophile that is prevented from attacking the metal center directly by its own steric demands or those imposed by the ligands about the metal can still access metal electron density that is delocalized onto the η^6-arene ligand. Indeed, protonation as it turns out is a fine probe of subtle differences between the sterics of different ancillary ligands. Such issues are particularly important for phosphine ligands which are frequently used as chiral ancillary ligands in asymmetric reactions that are catalyzed by metals.[60−63] Selectivity of such catalytic systems is largely dictated by the sterics of the ancillary ligands. Perhaps the most interesting aspect of the selectivity that is observed in the protonation of **1**−**5** is the fact that attack on the metal is not dictated strictly by the substitution patterns of the phosphine ligands. Thus, the derivative that is most readily attacked at the metal (**2**, the TRIPHOS derivative) arguably bears one of the more bulky phosphine ligands, whereas the derivative that bears presumably less bulky trialkylphosphine ligands (**5**, the PMe_3 derivative) still exhibits substantial amount of attack at the arene ligand.

It is clear that the conformations of unsymmetrically substituted phosphines about their M−P and P−C bonds play an important role in partitioning electrophilic attack on the metal versus the arene ligand. The conformations about the M−P bonds of some of the ligands are enforced by chelation. For example, the aryl substituents of the TRIPOD derivative **1** are forced in the direction of the η^6-arene ligand. On the other hand, no such conformational restrictions exist for the PPh_2-Me derivative **3**; yet essentially the same conformations about the M−P bonds of **1** and **3** are observed in their crystal structures, and calculations further suggest the conformation of **3** that is observed in the solid state is thermodynamically preferred. Accordingly, **1** and **3** exhibit the same reactivity pattern (100% attack on the arene ligand). Although the reactivity pattern of **2** may seem peculiar, space-filling models based upon the crystal structure of **2** suggest that ready access to the side of the molecule (between Mo−P(Ph)(CH_2^-)$_2$ and Mo−P(Ph)$_2$(CH_2^-) bonds) is possible (Figure 8, left), and this is confirmed in the surface electron density plots of Figure 8 (right). Semiempirical PM3(tm) calculations nicely predict essentially the conformations of **1**−**5** that are observed experimentally. Furthermore, mapping the occupied metal-containing frontier orbitals onto plots of the calculated surface electron density for **1**−**5** renders convenient models that predict the preferred sites of electrophilic attack (Figure 8, right). The electron density plots of **1** and **3** reveal no accessible metal electron density (except vis-à-vis their arene ligands). In contrast, electron density plots for **2**, **4,** and **5** suggest that direct access to metal electron density is possible for these species. Although these plots suggest that direct attack on the metal centers is possible, they do not predict the relative reactivities of **2**, **4**, and **5**. However, the CPK models clearly reveal increased steric accessibility to the metal centers in the order **4** < **5** < **2**, which happens to be the order of reactivity at the metal centers that is observed experimentally (as evidenced by the relative partitioning of attack at the metal versus attack at the arene ligand). Of considerable note is the plot for **2** that predicts attack at the metal to give the kinetic hydride $\mathbf{2_KH^+}$ and not the thermodynamic hydride $\mathbf{2_TH^+}$. Although even more surface frontier orbital electron density appears available between the two (−CH_2)P(Ph)$_2$ groups (Figure 8, right), that site is sterically shielded by the cleft formed by aryl substituents (Figure 8, left).

Dynamic Properties of $\mathbf{1H^+}$ and $\mathbf{2H^+}$. Complex $\mathbf{1H^+}$ exhibits C_s symmetry in solution and in the solid state.[9] Thus, the phosphine ligands are rendered chemically inequivalent. This is evidenced in the low-temperature ^{31}P NMR of $\mathbf{1H^+}$ that reveals a 2:1 ratio of phosphine resonances. A rate constant of 5.3×10^3 s^{-1} and activation barrier of $\Delta G^{\ddagger} = 35$ kJ mol^{-1} was measured for stereoisomerization of $\mathbf{1H^+}$ at the coalescence temperature of −70 °C. We have measured the same barrier for $\mathbf{1H^+}$-$\mathbf{d_7}$, suggesting no kinetic isotope effect for the stereoisomerization. The lack of an isotope effect and the preservation of ^{1}H/^{31}P coupling during isomerizations indicate an intramolecular process. There does not appear to be room in the pocket of the tripodal phosphine ligand of $\mathbf{1H^+}$ to accommodate the hydride ligand, so the barrier to isomerization is apparently associated with navigation of the hydride ligand between the Mo−P and Mo−arene groups. The rate constant of 6.4×10^3 s^{-1} and comparable activation barrier of $\Delta G^{\ddagger} = 31$ kJ mol^{-1} for interconversion of the two enantiomers of $\mathbf{2_KH^+}$ at the coalescence temperature of −87 °C indicate a similar process. However, the isomerization of $\mathbf{2_KH^+}$ to $\mathbf{2_TH^+}$ with a rate constant of

(60) *Asymmetric Catalysis*; Bosnich, B., Ed.; Martinus Nijhoff: Dordrecht, 1986.
(61) Kagan, H. B. In *Comprehensive Organometallic Chemistry*; Wilkinson, G., Stone, F. G. A., Eds.; Pergamon: Oxford, 1982; Vol. 8, pp 463−498.
(62) Noyori, R. *Science* **1990**, *248*, 1194.
(63) Ojima, I. *Pure Appl. Chem*. **1984**, *56*, 99.

6.1×10^{-4} s^{-1} and an activation barrier of $\Delta G^{\ddagger} = 65$ kJ mol^{-1} at −60 °C appears quite different. We attribute the higher barrier of the stereoisomerization of $\mathbf{2_K H^+}$ to $\mathbf{2_T H^+}$ compared with stereoisomerization of $\mathbf{2_K H^+}$ to steric factors. The CPK model of **2** clearly reveals a gap between the arene ligand and the M−P(Ph)(CH_2^-)$_2$ bond, but no such gap exists between the arene ligand and the M−P(Ph)$_2$(CH_2^-) bonds.

Quantification of Steric Effects. The relationship between structure and reactivity[64] and the concept of steric hindrance[65] have been recognized for more than a century. In the interim there have been may attempts to quantify steric effects. The approaches may be classified as (1) direct physical measurement via metric data, (2) inference of relative size from trends in reactivity, and (3) the use of molecular mechanics and/or molecular orbital models. Perhaps the most widely applied measure of sterics in organometallic chemistry (and an example of the first approach) is the "cone angle" (θ) introduced by Tolman as a means of describing the steric requirements of phosphine ligands.[66,67] Rules were later developed to deal with nonaxial substituents and unsymmetrically substituted phosphines. Thus, the values of θ for PMe_3, $PPhMe_2$, and PPh_2Me are 118°, 122°, and 136°, respectively. This is the same trend that we observe in the reactivities of **3**−**5** toward protons. Although Tolman's original definition of θ was based on a "hard sphere" model, it is well recognized that steric and electron factors are both important,[68] and these factors are frequently inextricably commingled. Since Tolman's first effort to quantify the steric requirements of phosphine, there have been many modifications to Tolman's original parameters. For example, Stahl and Ernst[69] corrected θ based on experimental bond dissociation enthalpies in bis(2,4-dimethylpentadienyl)titanium complexes, and Mosbo et al. made related corrections using computed geometries and heats of formation.[70] Both of these studies reported the same trend for PMe_3 and $PPhMe_2$, but PPh_2Me was not considered. The relative ordering of monodentate phosphine ligands according to their steric requirements is relatively straightforward, and many reactivity trends can be understood using such models. Although the steric demands for bidentate phosphine ligands have been modeled by the Tolman method,[66,67,71,72] and such treatments have proven valuable in predicting reactivity trends,[73] to our knowledge no such analysis of tridentate phosphine ligands has been attempted. The present study in effect makes use of all three approaches (vide supra) to evaluate the steric environments about the metal centers of **1**−**5**. We conclude for the following reasons that, in the absence of dominating steric effects, attack by protons on the metal is favored over attack on the arene ligand, and equatorial attack on (η^6-arene)-Mo(P)$_3$ is preferred over axial attack:

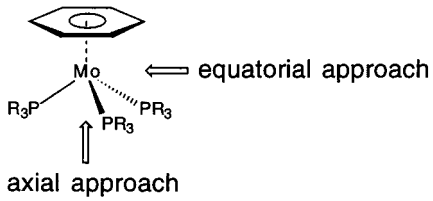

1. Derivatives **1** and **3** exhibit comparable orientations about their Mo−P bonds and, therefore, similar equatorial steric environments. The axial approach is blocked by the TRIPOD backbone in the case of **1** and comparatively open in the case of **3** (cf. **5**). Nonetheless, **1** and **3** are both attacked 100% at the arene, which indicates a preference for attack at the arene ligand rather than axial attack in the cases where equatorial approach is hindered. 2. The reactivity trends of **3**−**5** follow the steric nature of the substituents in the equatorial plane ((Ph)$_2$ vs (Ph)(Me) vs (Me)$_2$). 3. Unlike the C_3 symmetry of **4** that orients one Ph substituent along each of the three possible equatorial trajectories, the C_1 symmetry of **2** allows the $-CH_2P(Ph)CH_2-$ moiety to block approach from only one side, leaving the other side exposed (cf. Figure 2):

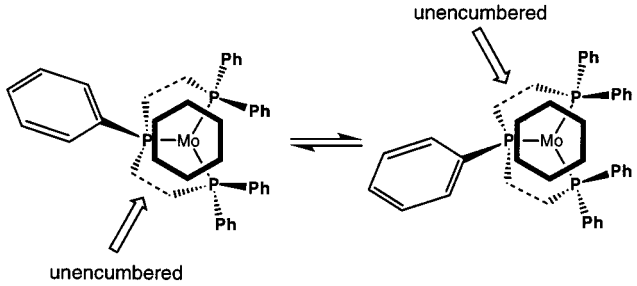

The axial approach is relatively unencumbered for **2**, once again suggesting an electronic preference for equatorial attack. Accordingly, both steric and electronic factors play important roles in determining the kinetic sites of protonation of **1**−**5**.

Conclusions

We conclude from the crystal structures of **1**−**4**, tracer studies, and electronic structure calculations for the five derivatives **1**−**5** presented herein that the steric demands of the phosphine ligands play an important role in dictating whether a proton attacks the arene ligand or the metal of **1**−**5**. A priori prediction of the relative steric requirements of the phosphine ligands that have been employed in this study is a challenge (cf. the TRIPHOS and PMe_3 derivatives). However, mapping the metal-based frontier orbitals of the complexes **1**−**5** onto plots of their surface electron density (thereby revealing sterically accessible metal electron density) calculated using the semiempirical PM3(tm) method and geometries derived from both the crystal structure coordinates (for **1**−**4**) and geometries that were optimized using the PM3(tm) method (for **1**−**5**) provides a straightforward model that predicts the mechanisms of attack by protons.

(64) Hofmann, A. W. *Chem. Ber.* **1872**, *5*, 704.
(65) Meyer, V. *Chem. Ber.* **1894**, *27*, 510.
(66) White, D.; Coville, N. J. *Adv. Organomet. Chem.* **1994**, *36*, 95−158.
(67) Tolman, C. A. *Chem. Rev.* **1977**, *77*, 313.
(68) For an excellent example of ancillary ligands influencing the relative importance of electronic (i.e., pK_b) and steric (i.e., θ) factors see: Geno, M. K.; Halpern, J. *J. Am. Chem. Soc.* **1987**, *109*, 1238.
(69) Stahl, L.; Ernst, R. D. *J. Am. Chem. Soc.* **1987**, *109*, 5673.
(70) DeSanto, J. T.; Mosbo, J. A.; Storhoff, B. N.; Bock, P. L.; Bloss, R. E. *Inorg. Chem.* **1980**, *19*, 3086.
(71) Casey, C. P.; Whiteker, G. T. *Isr. J. Chem.* **1990**, *30*, 299.
(72) Casey, C. P.; Whiteker, G. T.; Campana, C. F.; Powell, D. R. *Inorg. Chem.* **1990**, *29*, 3376.
(73) Casey, C. P.; Whiteker, G. T.; Melville, M. G.; Petrovich, L. M.; Gavney, J. A., Jr.; Powell, D. R. *J. Am. Chem. Soc.* **1992**, *114*, 5535.

Acknowledgment. The financial support of the National Science Foundation (CHE-9612869) and the Oklahoma Center for the Advancement of Science and Technology (OCAST HR98-078) is gratefully acknowledged.

Supporting Information Available: Thermal ellipsoid drawing of **2** showing its disorder; tables of atomic coordinates and equivalent isotropic displacement parameters, anisotropic displacement parameters, hydrogen coordinates and isotropic parameters, bond lengths and angles for **1**−**4**, and representative spectra. X-ray crystallographic files for **1**−**4**, in CIF formats, are available through the Internet only. This material is available free of charge via the Internet at http://pubs.acs.org.

OM990281N